Draft version September 23, 2025
Typeset using LaTeX **default** style in AASTeX7

Revealing the accelerating wind in the inner region of colliding-wind binary WR112

John D. Monnier [1], Yinuo Han [2], Michael F. Corcoran [3,4], Sanne Bloot [5,6], Joseph R. Callingham [5,7], William Danchi [8], Philip G. Edwards [9], Lincoln Greenhill [10], Kenji Hamaguchi [3,11], Matthew J. Hankins [12], Ryan Lau [13], Jon M. Miller [1], Anthony F. J. Moffat [14], Garreth Ruane [15], Christopher M. P. Russell [16], Anthony Soulain [17], Samaporn Tinyanont [18], Peter Tuthill [19], Jason J. Wang [20] and Peredur M. Williams [21]

[1] *Astronomy Department, University of Michigan, Ann Arbor, MI 48109, USA*
[2] *Division of Geological and Planetary Sciences, California Institute of Technology, 1200 E. California Blvd., Pasadena, CA 91125, USA*
[3] *CRESST II and X-ray Astrophysics Laboratory, NASA/Goddard Space Flight Center, Greenbelt, MD 20771, USA*
[4] *The Catholic University of America, 620 Michigan Ave., N.E. Washington, DC 20064, USA*
[5] *ASTRON, Netherlands Institute for Radio Astronomy, Oude Hoogeveensedijk 4, Dwingeloo, 7991 PD, The Netherlands*
[6] *Kapteyn Astronomical Institute,University of Groningen, P.O. Box 800, 9700 AV, Groningen, The Netherlands*
[7] *Anton Pannekoek Institute for Astronomy, University of Amsterdam, Science Park 904, 1098 XH Amsterdam, The Netherlands*
[8] *NASA Goddard Space Flight Center, Astrophysics Division, Greenbelt, MD, 20771, USA*
[9] *CSIRO Space and Astronomy, Australia Telescope National Facility, PO Box 76 Epping 1710, NSW, Australia*
[10] *Harvard-Smithsonian Center for Astrophysics, 60 Garden Street, Cambridge, MA 02138,*
[11] *Department of Physics, University of Maryland, Baltimore County,1000 Hilltop Circle, Baltimore, MD 21250, USA*
[12] *Arkansas Tech University, 215 West O Street, Russellville, AR 72801, USA*
[13] *NSF NOIRLab, 950 N. Cherry Ave., Tucson, AZ 85719, USA*
[14] *Département de physique, Université de Montréal, 1375 Avenue Thérèse-Lavoie-Roux, Montréal (QC), H2V 0B3, Québec, Canada*
[15] *Jet Propulsion Laboratory, California Institute of Technology, Pasadena, California, USA*
[16] *Department of Physics and Astronomy, Bartol Research Institute, University of Delaware, Newark, DE, 19716, USA*
[17] *Univ. Grenoble Alpes, CNRS, Alpes, Grenoble, France*
[18] *National Astronomical Research Institute of Thailand, 260 Moo 4, Donkaew, Maerim, Chiang Mai, 50180, Thailand*
[19] *Sydney Institute for Astronomy University of Sydney, NSW 2006, Australia*
[20] *Center for Interdisciplinary Exploration and Research in Astrophysics (CIERA) and Department of Physics and Astronomy, Northwestern University, Evanston, IL 60208, USA*
[21] *Institute for Astronomy, University of Edinburgh, Royal Observatory, Edinburgh, EH9 3HJ, UK*

ABSTRACT

Colliding winds in massive binaries generate X-ray–bright shocks, synchrotron radio emission, and sometimes even dusty "pinwheel" spirals. We report the first X-ray detections of the dusty WC+O binary system WR 112 from Chandra and Swift, alongside 27 years of VLA/ATCA radio monitoring and new diffraction-limited Keck images. Because we view the nearly circular orbit almost edge-on, the colliding-wind zone alternates between heavy Wolf-Rayet wind self-absorption and near-transparent O-star wind foreground each 20-yr orbit, producing phase-locked radio and X-ray variability. **This scenario leads to a prediction that the radio spectral index is flatter from a larger non-thermal contribution around the radio intensity maximum, which indeed was observed.** Existing models that assume a single dust-expansion speed fail to reproduce the combined infrared geometry and radio light curve. Instead, we require an accelerating post-shock flow that climbs from near-stationary to ∼1350 km/s in about one orbital cycle, naturally matching the infrared spiral from 5" down to within 0."1, while also fitting the phase of the radio brightening. These kinematic constraints supply critical boundary conditions for future hydrodynamic simulations, which can link hot-plasma cooling, non-thermal radio emission, X-ray spectra, and dust formation in a self-consistent framework. WR 112 thus joins WR 140, WR 104, and WR 70-16 (Apep) as a benchmark system for testing colliding-wind physics under an increasingly diverse range of orbital architectures and physical conditions.

Email: monnier@umich.edu

Keywords: Wolf-Rayet stars (1806) — WC Stars (1793) — Stellar Winds (1636) — Circumstellar Dust (236) — High energy astrophysics (739) — Close binary stars (254)

1. INTRODUCTION

Cosmic dust is essential for the formation of low-mass stars and habitable planets. We find dust forming in a variety of stellar environments: explosive outbursts (novae and supernovae), slow-moving stellar outflows (red giant and supergiant winds), and in the fast winds of classical, hot, carbon-rich Wolf-Rayet (WR) stars (the evolved descendants of massive O-type stars). In almost all of these outflows, dust production occurs under density, pressure and chemical conditions that are poorly constrained.

The production of dust in Wolf-Rayet systems is a particular mystery, since Wolf-Rayet stars have $T_{\rm eff} \sim 50,000$ K and thus are strong sources of photo-ionizing, dust-destroying UV radiation – yet somehow dust is able to form within this harsh environment. Dust formation in WR stars seems to require not only a C-rich (WC-type) WR star, but quite likely also the presence of a binary companion in which the dust forms in the highly condensed colliding-wind zone between the two stars, although large clumping in turbulent winds might also trigger dust formation in some single WC stars (e.g., A. David-Uraz et al. 2012).

Dust producing Wolf-Rayet binaries thus are especially important laboratories for studying the conditions needed for dust to condense, as we can find systems with different mass-loss rates and physical separations to explore the physics behind the dust formation process. We often see patterns that repeat on the orbital period, allowing detailed study and follow-up. Most identified dust-producing WR binaries consist of a chemically evolved, carbon-rich Wolf-Rayet star, possessing a strong, dense radiatively-driven stellar wind ($\dot{M} \gtrsim 10^{-6}$ $M_\odot$ yr^{-1}, $V_\infty \sim 1000 - 3000$ km s^{-1}) gravitationally bound to a massive (typically O-type) companion with a similarly fast (though less dense) radiatively-driven stellar wind. The stellar winds from the two stars collide hypersonically, producing a strong, dense, extremely hot ($T > 10^7$ K) "bow shock", which emits in the thermal X-ray band (0.5 – 10 keV). The carbon-rich wind of the WR star is compressed in the colliding wind shock, and somehow the gas cools enough and remains dense enough that PAH molecules in some cases (S. V. Marchenko et al. 1997), carbon chains and amorphous carbon grains can form at a significant rate ($\sim 10^{-10} - 10^{-6}$ M$_\odot$ yr^{-1}, R. M. Lau et al. 2020). X-ray emission from the shock provides our only direct measure of the thermodynamic conditions (densities, temperatures, pressures and abundances) in the hot shocked gas, the precursor to dust formation. Non-thermal emission in the radio and X-ray regimes is also associated with this colliding wind zone (e.g., J. P. Moran et al. 1989; R. L. White & R. H. Becker 1995; K. Hamaguchi et al. 2018).

Much of the above picture was worked out from infrared, radio and X-ray observations of WR 140, a highly-eccentric binary in a 8-yr orbit where dust is formed only near periastron passage (P. M. Williams et al. 1990). Although the basic theory of colliding stellar winds was first understood in the 1990s (V. V. Usov 1991; I. R. Stevens et al. 1992), we still struggle to fit the full WR 140 dataset, such as the time variable non-thermal radio emission (R. L. White & R. H. Becker 1995) and X-ray properties (A. M. T. Pollock et al. 2021) due to uncertainties in orbit, difficulty making unambiguous X-ray and non-thermal radio predictions from hydrodynamical models, and complications from the time-variable line-of-sight wind opacity in the dynamic circumstellar environment.

We can learn even more by combining radio and infrared photometry with diffraction-limited infrared imaging. P. G. Tuthill et al. (1999) made the unexpected discovery that the WC+O binary WR 104 looked like a spinning spiral on the sky, the first pinwheel nebula. Later, WR 98a, WR 112 and others (J. D. Monnier et al. 1999, 2007) were added to this list, along with their radio properties (J. D. Monnier et al. 2002). Despite the clear evidence for colliding winds in this system, none of the *persistent* dust emitters had been detected in X-rays in surveys: The X-ray luminosity was lower than seen in more widely-separated colliding wind system WR140 (at apastron) and possibly more similar to the dust-free, close-in WR binary γ^2 Vel (P$\sim$79 days).

The Wolf-Rayet binary WR112 is a particularly important example of a dust-producing long-period colliding wind binary. While its period was first thought to be only a few years since it was a persistent dust-emitter, subsequent monitoring determined the period was much longer, around 20 years (R. M. Lau et al. 2020). Here we collect decades of unpublished radio and infrared monitoring along with the first X-ray detection to peer deeply into the inner regions of this colliding wind system. In §2, we present our current picture of WR 112 based largely on mid-infrared imaging. In §3, we present the first X-ray detections of WR112 by the Chandra X-ray Observatory and the Neil Gehrels Swift Observatory, long-term radio monitoring from VLA and ATCA, multi-epoch diffraction-limited imaging with Keck

Table 1. Geometrical parameters of the colliding wind model for WR 112.

	R. M. Lau et al. (2020)	this work
Binary Period P [yr]	$19.4^{+2.7}_{-2.1}$	20.0±0.1
Inclination i [°]	100 ± 15	unchanged
Longitude of asc. node Ω [°]	-15 ± 10	unchanged
Eccentricity e	0	see §4
Cone half-opening angle θ_w [°]	55 ± 5	unchanged
Distance (kpc)	3.39	unchanged

aperture masking, and lastly a Keck adaptive optics image behind the vortex coronagraph. In §4, we extend the mid-infrared dust shell modeling to the inner region of the nebula (< 1") where we confront existing models with new data, finding severe discrepancies. Here we compare our findings for WR112 with the prototypical colliding-wind binary WR 140. We then close with a brief set of conclusions in §5.

2. THE WR 112 BINARY AND COLLIDING-WIND MODEL

WR 112 was first identified as a bright IR source from sounding-rocket observations made more than 40 years ago (M. Cohen & S. N. Vogel 1978) and its dust shell was resolved by lunar occultation (S. Ragland & A. Richichi 1999). This "persistent" dust emitter was first imaged in the mid-infrared by the Gemini telescope, revealing the presence of nested, extended, asymmetric dust arcs (S. V. Marchenko et al. 2002). These shells were erroneously interpreted as a face-on spiral, while radio and near-IR imaging would point to an edge-on geometry (J. D. Monnier et al. 2002, 2007). R. M. Lau et al. (2020) settled the issue by detecting clear proper motions of the dust arcs from multiple mid-infrared images spanning most of the $P = 19.4 \pm 3$ yr orbital period. Although the binary itself has not been resolved yet, a 3-dimensional model of the dust was presented that suggests a nearly circular orbit with an inclination of $i = 100°$ (see Figure 1). Other long-period WC binaries have high orbital eccentricities and tend to produce dust episodically only for some defined interval around periastron passage, while WR 112 continually produces dust (P. M. Williams 1995) with constant infrared flux, suggesting a close-to-circular orbit.

The rate of dust production in WR 112 has been best measured as M_d =2.7×10^{-6} $M_\odot$ yr^{-1} by modeling of the dust arcs for an assumed distance of 3.4kpc (R. M. Lau et al. 2020, see Figure 1). This is a much larger rate than the dust production rate of almost any other long-period WR binary previously studied (R. M. Lau et al. 2020), and comparable to that of WR104 (P. G. Tuthill et al. 1999), a short period ($P = 0.6$ yr) system which has a dust production rate of 4.4×10^{-6} $M_\odot$ yr^{-1}. Dust production for the eccentric WR140 binary system is strongly suppressed at wide separation, which makes it intriguing that WR 112 is such a prodigious dust producer. The observed dust formation rate means that about 8% of the wind of the WC star in WR 112 is converted to dust. The dust is consistent with amorphous carbon grains with a typical grain size $0.1 - 1.0\,\mu$m (S. V. Marchenko et al. 2002; R. M. Lau et al. 2020).

The wind of the WC star in WR 112 has a terminal velocity $V_{\infty,\mathrm{WC}} \sim 1230 \pm 260$ km s^{-1}, and a large wind-driven mass-loss rate, $\dot{M}_{\mathrm{WC}} \sim 1.1 \times 10^{-4}$ $M_\odot$ yr^{-1} (R. M. Lau et al. 2020), while the companion (assumed to be an early-O supergiant) probably has a higher wind velocity, $V_{\infty,\mathrm{O}} \sim 2000$ km s^{-1}, with a lower mass loss rate, $\dot{M}_{\mathrm{O}} \sim 8 \times 10^{-6}$ $M_\odot$ yr^{-1}. At these velocities the thermalization temperature in the shock is ~ 60 MK, with an expected luminosity of $\sim 10^{33}$ ergs s^{-1} or so (for comparison, the system has a bolometric luminosity $L_{bol} \approx 1.5 \times 10^{39}$ ergs s^{-1}). Thus we need to also understand the thermodynamic conditions of the hot X-ray emitting gas in the colliding wind shock in order to fully understand how the colliding wind shock in WR 112 produces dust so efficiently. This requires measurement of the X-ray spectrum, since the X-ray spectrum probes the local conditions of the hot shocked gas near the point of impact, free from contamination of other sources of emission associated with the stars or their winds.

Table 1 contains the overall geometry assumed for this paper based on modeling of the mid-infrared imaging.

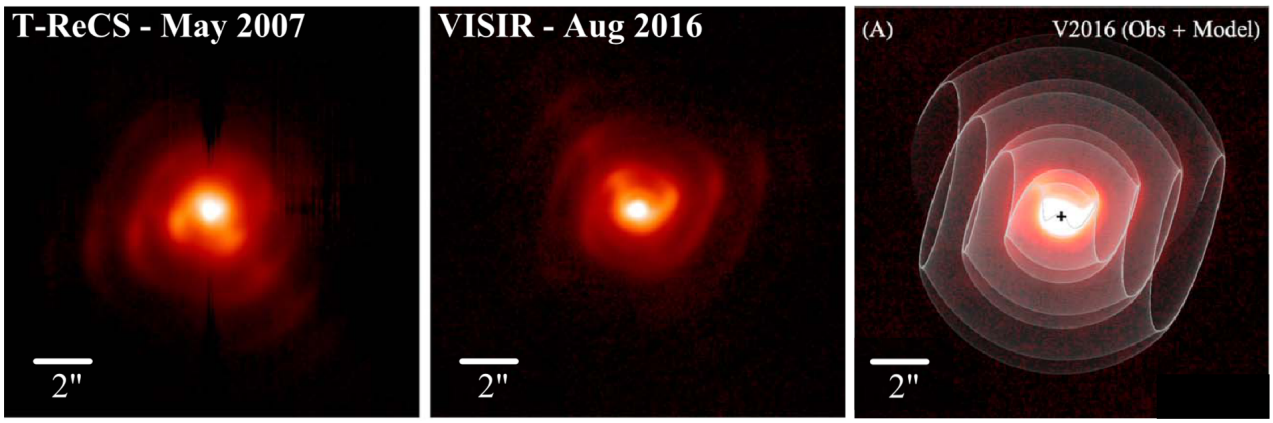

Figure 1. WR 112 N-band ($\lambda \sim 12\mu$m) images from 2 epochs (adapted from Figs. 2 & 3 of R. M. Lau et al. 2020). Note the different orientations of the U-shaped structures within 2″ of the central binary, indicative of orbital motion. The rightmost figure shows a dust model applied to the 2016 N-band image. Orbital motion and the expansion of the dust arcs in the wind from WR 112 reproduces the observed spatial distribution of the inner and outer dust arcs projected on the sky.

Table 2. X-ray Observations of WR 112

Facility ID	Start	End	Exposure	L_X
			s	10^{33} erg s^{-1}
Swift 00014039002	2021-02-15T04:57	2021-02-15T05:11	849.08	1.8±0.6
Swift 00014039003	2022-05-04T20:12	2022-05-04T20:41	1730.61	2.9±0.5
Swift 00014039004	2022-05-05T01:05	2022-05-05T02:59	1855.49	2.0±0.4
Swift 00014039005	2022-05-08T15:21	2022-05-09T23:14	3024.25	2.5±0.3
Swift 00014039006	2022-09-29T02:56	2022-09-29T23:52	5009.59	1.0±0.3
CHANDRA 25129	2023-07-03T23:00	2023-07-04T04:37	17840.89	1.28±0.01
CHANDRA 27939	2023-07-04T10:47	2023-07-04T16:07	16748.81	1.18±0.04

3. OBSERVATIONS

3.1. *X-ray imaging and spectra*

3.1.1. *Neil Gehrels Swift Imaging Observations*

Unfortunately, few X-ray observations of WR 112 exist. X-ray emission from a source about 8.1″ from the known position of WR 112 was made in a short (853 s) exposure with the Neil Gehrels *Swift* X-ray Telescope (XRT) in photon-counting mode as part of a Director's Discretionary Time observation. This short exposure only detected 15 counts over the full XRT energy band **(0.2 –10 keV, approximately)**. At the assumed distance of WR 112 (3.4 kpc) the XRT count rate corresponds to a substantial X-ray luminosity, $L_x \approx 1.8{\times}10^{33}$ ergs s^{-1}. **In 2022, the field centered on WR 112 was observed four additional times with the Swift XRT in photon-counting mode, confirming the detection of this source**. Table 2 lists these observations, along with the estimated observed X-ray luminosity at each epoch. The position of the *Swift*-XRT source was read off the *Swift* XRT image as $\alpha = 18h16m33.3s$, $\delta = -18°58'34.7''$, which is about 8″ from the 2mass J-band location of WR 112. **We also ran the `wavdetect` source detection tool (available through the Chandra CIAO analysis package) on the deepest Swift image, using initial wavelet scales of 2, 4, and 8 pixels. This analysis returns a source position of $\alpha = 18h16m33.6s$, $\delta = -18°58'41.5''$, with a statistical error of about 0.6 arc seconds. This is formally 1.5″ from the known location of WR 112, though systematic uncertainty in absolute alignment of the XRT image could not be quantified due to lack of other strong X-ray sources in the field.**

3.1.2. *The CHANDRA Observations*

In order to confirm that the *Swift* source was in fact WR 112, we observed the region around WR 112 on 2023 July 3 – 4 with *CHANDRA*. **A list of the particular Chandra datasets can be accessed in DOI: X.** We reprocessed the *CHANDRA* observations using the `chandra_repro` python module distributed as part of the `ciao_contrib.runtool` package, distributed with version 4.15.1 of the `ciao` analysis package. Table 2 also summarizes the two *CHANDRA* pointings. The exposure time of the first observation segment, ObsID 25128 was 17.8 ks, while the exposure time of the second observation segment, ObsID 27939. was 16.7 ks.

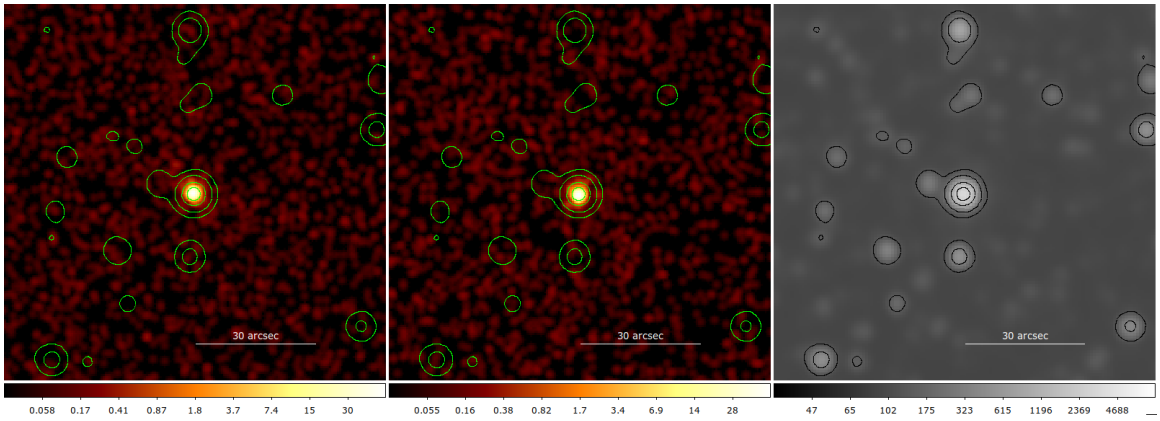

Figure 2. Left: False-color Broad-band (0.2 –10 keV) *CHANDRA* image of the WR 112 field from ObsID 25129; Center: *CHANDRA* image, ObsID 29739; Right: 2MASS J-band ($\lambda \sim 1.23\mu$m) image of WR 112. Contours from the 2MASS image are overlaid on the *CHANDRA*images. Note that, aside from WR 112, there are no other J-band sources clearly detected in the *CHANDRA* X-ray images.

Figure 2 compares a broad-band (0.2 – 10 keV) image of the WR 112 field from the *CHANDRA* observation ObsID #25129, the 18 ksec observation, and the *CHANDRA* image from ObsID 29739 with a J-band image from the 2MASS survey. An alignment correction of 0.5″ was applied to ObsID #29739 to align the strong X-ray source in each X-ray image. The brightest source in the 2MASS J-band image is WR 112. Contours from the 2MASS J-band image are superimposed on the J-band image and on the two X-ray images. The WR 112 J-band contour is well aligned with the strongest source in the *CHANDRA* X-ray images, confirming WR 112 as the X-ray source. Figure 3 shows the 0.1 – 10 keV band net count rates for WR 112 extracted from the *CHANDRA* observations. Source counts were extracted from a 12″ diameter circle centered on WR 112, and background was extracted from a circular source-free region of 51″ centered at $\alpha = 18h : 16m : 38s$, $\delta = -18°{:}58'{:}14''$. No obvious short-timescale variability is seen.

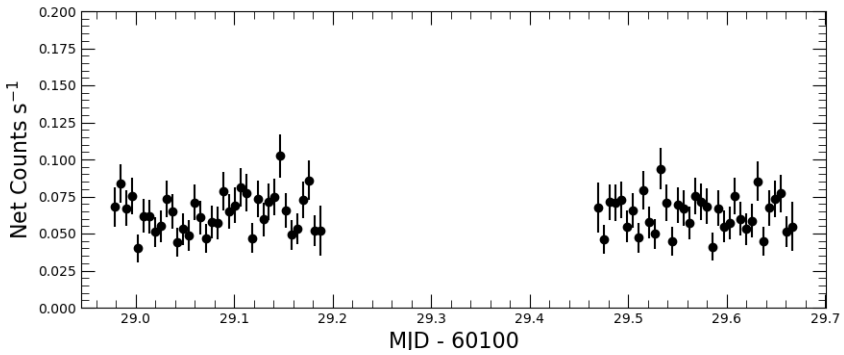

Figure 3. The 0.1 – 10 keV band *CHANDRA* X-ray lightcurve of WR 112, using 500 second bins.

We extracted spectra from Obsids 25129 and 27939 from circular regions of 12″ centered on the optical position of WR 112. Backgrounds were extracted from nearby source-free regions. We created redistribution matrix files (rmfs)

Table 3. X-ray Spectral Parameters Derived from the Chandra Spectrum Analysis

Parameter	Value
$N_{\rm H}$ (10^{22} cm^{-2})	$3.0^{+0.5}_{-0.3}$
kT (keV)	0.5 ± 0.2
EM (10^{56} cm^3)	3^{+7}_{-1}
kT (keV)	2.0 ± 0.2
EM (10^{56} cm^3)	2.4 ± 0.4
$A_{\rm Fe}$	$0.4^{+0.2}_{-0.1}$
unabsorbed L_x (10^{33} ergs s^{-1}, 1 – 10 keV)	4.9 ± 0.5
Cash stat.	65.7
Deg. of freedom	56

and ancillary response files (arfs) for each Obsid using the CIAO (A. Fruscione et al. 2006) `specextract` tool. The individual spectra were revealed to be fully consistent in simple fits, so we added the spectra using the CIAO tool `combine_spectra`. The combined spectrum was then binned using the "optimal" binning algorithm of J. S. Kaastra & J. A. M. Bleeker (2016), and fit over the 1–8 keV band using XSPEC version 12.14.1 (K. A. Arnaud 1996). The fits minimized a Cash statistic (W. Cash 1979).

We initially fit the combined spectrum using a simple single-temperature plasma model, modified by neutral gas absorption (`tbabs`×`apec`). This simple model provides an adequate fit ($C = 88$ for 59 degrees of freedom), but leaves residuals in the vicinity of He-like Si XIII (1.87 keV). We therefore added a second plasma component and our spectral fit is shown in Figure 4. This yielded an improved fit ($C = 73$ for 57 degrees of freedom), and accounted for the potential Si XIII flux. This model over-predicts He-like Fe XXV at 6.70 keV. Replacing the simple plasma models with counterparts that have variable abundances (`tbabs`×`vapec`+`vapec`) further improved the fit when the abundance of Fe is allowed to drift to sub-solar values ($C = 66$ for 56 degrees of freedom).

The X-ray luminosity in the 1 – 10 keV band is comparable to the luminosity of other WC-type colliding wind binaries, and is roughly equivalent to the X-ray luminosity of WR 140 when that binary is far from periastron passage (A. M. T. Pollock et al. 2021). The derived column density is also similar to the column to WR 140, when the star is far from periastron and absorption by the WC7 wind is unimportant. Lastly, we note that the high temperature component (kT∼2keV) is compatible with the expected shock temperature of the WC wind given its terminal speed (1230 km/s).

3.2. *Radio light curve*

Radio observations of WR 112 have been obtained from 1995 to 2022. These include 171 flux density measurements not reported before by the principal investigators of those programs, and 15 previously published observations. We note that some of the datasets presented here were analyzed from the Karl G. Jansky Very Large Array (VLA) archive and reported on by J. O. Yam et al. (2015), though our results here are independent and do not refer to this parallel effort.

In all observations, the radio emission was unresolved and here we report only flux measurements in a variety of bands, though mostly at X-band (3.6cm, 8GHz). The detailed data analysis procedures were outlined in J. D. Monnier et al. (2002) and followed throughout the observing campaign. The older VLA data were analyzed using AIPS while the newer JVLA and ATCA data reduction employed CASA (CASA Team et al. 2022). The main VLA flux amplitude calibrator was 3C286 while 1733-130, 1751-253, and 1832-105 were used for nearby phase calibrators. The JVLA data taken after 2015 were calibrated with the standard VLA calibrator pipeline, with 3C286 as the amplitude calibrator and J1820-2528 as the phase calibrator. For ATCA observations, the amplitude calibrator was PKS B1934-638 for the observations taken in 2020 and 2021. For the observation on 2022-03-06, PKS B1934+638 was used as the amplitude calibrator for C- and X-band, while PKS B1921-293 was used for the K-band data. PKS B1730-130 was used as the phase calibrator.

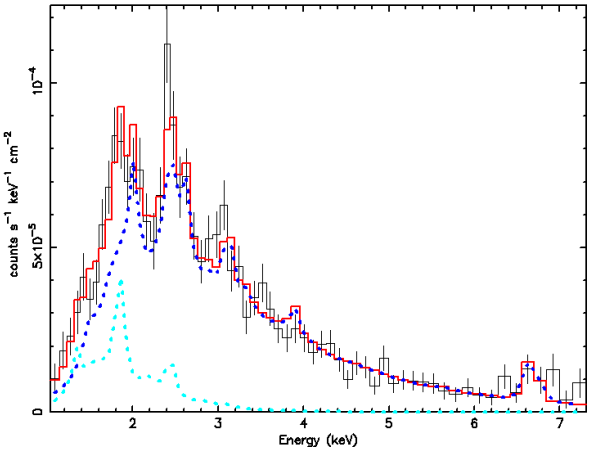

Figure 4. The summed Chandra ACIS X-ray spectrum of WR 112. The data are binned for visual clarity. The best-fit two-temperature plasma model is shown in red (`tbabs`×`vapec`+`vapec`). The kT= 0.5 keV and kT= 2 keV components are shown in cyan and blue, respectively. The strongest lines in the model are He-like Si XIII, S XVI, Ar XVII, and Fe XXV (1.87, 2.46, 3.14, and 6.70 keV, respectively). The spectrum is obscured at low energy by the high line-of-sight column density. See Table 3 for model parameters and errors.

Almost all the radio epochs include an 8GHz measurement, and the 8GHz flux curve is shown in Figure 5 (left panel). Note that the error bars are not included in the plot as they are typically smaller than the plot symbol. When multiple wavelengths were available for a given epoch, we fit a simple power law model, $F_\nu = F_{8\mathrm{GHz}}(\frac{\nu}{8\mathrm{GHz}})^\alpha$, between 2 and 25 GHz. Based on earlier work (e.g., J. D. Monnier et al. 2002), we expect a thermal (free-free) spectrum ($\alpha \sim 0.6$) when WR 112 is in the low state since the non-thermal radio emission from the colliding wind shock is buried behind the dense WR wind. When the shock front is visible through the weaker O-star wind, we expect to see stronger radio flux with a flat spectrum ($\alpha \sim 0$) characteristic of non-thermal synchrotron emission. Figure 5 (right panel) shows the correlation between spectral index and flux density. Using this derived correlation, we synthesized 8 GHz flux estimates for observations missing measurements at 8 GHz. These points are included in the 8 GHz flux density curve shown in Figure 5 (left panel). The full dataset with flux density measurements at all epochs (including error bars) and bands can be found in appendix A.

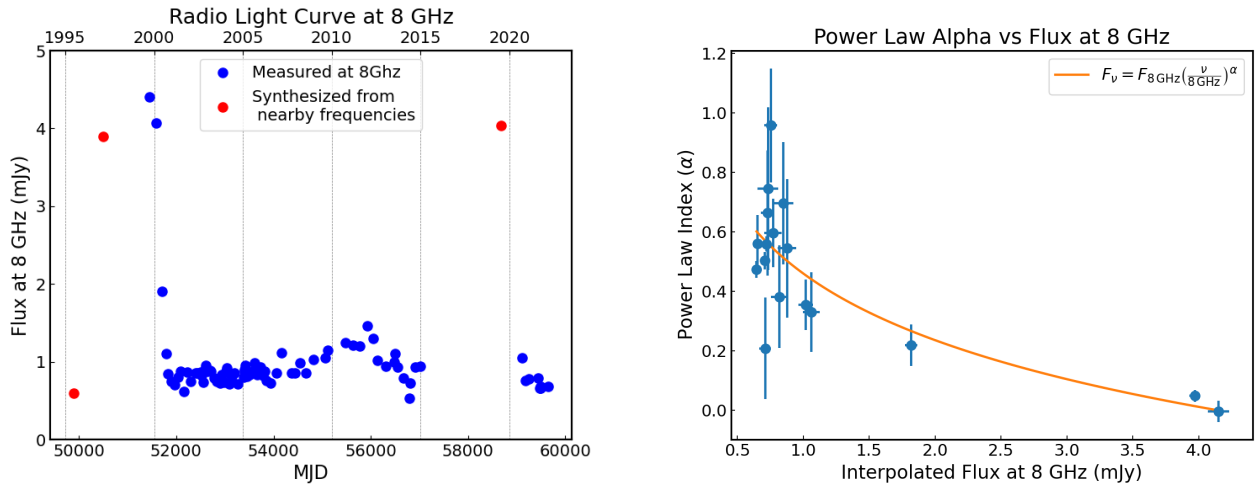

Figure 5. Left: The 8 GHz light curve of WR112, including synthesized flux estimates when only nearby frequencies were available. Right: The spectral index correlation with flux, as WR 112 transitions from the "high state" dominated by non-thermal radio emissions to the "low state" where we only see thermal (free-free) emission from the ionized winds.

This long-term monitoring program began after J. D. Monnier et al. (2002) highlighted the strong variability in WR 112 radio light curve based on the earlier data of C. Leitherer et al. (1997) and J. M. Chapman et al. (1999). The flux declined from 4mJy down to <1mJy between 2000 February and 2000 October, accompanied by a dramatic change in the spectral index. Because the binary separation is too small to resolve directly, and the orbital velocities too low to determine a radial velocity curve, constraining even the orbital period was difficult. Continued monitoring of the radio flux density offered the possibility of determining the orbital period of the binary, as had been done for WR 140 by R. L. White & R. H. Becker (1995). Further, the percentage of the time the system is in the "high state" compared to the "low-state" can help constrain the inclination of the system and also the opening angle of the colliding wind shock. Based on earlier radio and dust observations of WR 140, we expected the period to be at most a few years.

We began a monitoring campaign which lasted for 15 years without return of the original radio high state, and the VLA monitoring was terminated in 2015. The small rise in the radio emission in 2012–2013 was suspected as being due to a partial return to maximum light (not true) but it was unclear at the time. A renewed monitoring effort began in 2020 following an estimate of the orbital period of $19.4^{+2.7}_{-2.1}$ yrs from R. M. Lau et al. (2020) based on the proper motion of mid-infrared dust shells.

While our new monitoring began too late to catch the radio high state (as confirmed by one 2019 measurement by the VLASS all-sky survey; Y. A. Gordon et al. 2021), the photometry shows that an observation on 2020 Sep 15, with an elevated flux above 1mJy, matches closely a similarly elevated flux observed on 2000 Sep 08, almost 20 years earlier. Assuming that the radio flux curve repeats itself exactly every orbit, these two observations suggest that the radio period is 20.0 ± 0.1 yrs, consistent with the period derived by R. M. Lau et al. (2020) in the mid-IR. We note again the statistically-significant rise in radio brightness around 2012 that we can not currently explain, but might be understood with additional modelling.

The phased light curve is shown in Figure 6 with an arbitrary T_0 = 2007 Jan 01 (MJD 54101.0) and $P = 20.0 \pm 0.1$ yrs. The onset of the next high state should occur between 2035 and 2037 and the high state should last ∼3 – 5yrs (15% – 23% of the orbit). Note that the inclination of the system given in §2 is 100±15° (so that the line-of-sight is nearly in the orbital plane). The cone half-opening angle is believed to be 55° **(see Table 1)**, which would naively suggest a ∼30% duty-cycle when the line-of-sight traverses the weaker O-star wind into the non-thermal radio emitting region. The slight discrepancy in the measured duty cycle is likely due to a lower orbital inclination which would reduce the fraction of the time the system is viewed in the high-state. **Interestingly, we will show later in this paper that the phasing of the radio light curve is far different than expected from the canonical wind model, and that will be key to deriving new model constraints on the wind acceleration to be discussed in §4.**

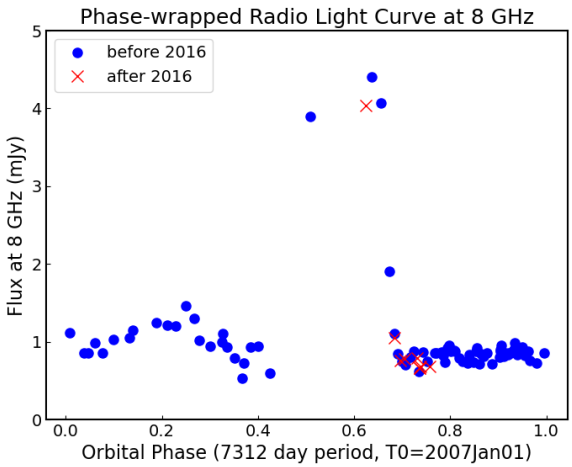

Figure 6. The phased-up 8 GHz light curve for WR112 (including synthesized flux estimates when only nearby frequencies were available) compared to orbital phase, assuming a period of 7312 days (20.0yrs). The data before 2016 are marked with circles while data after marked with crosses to show the level of repeatability.

Table 4. Keck Observatory Observing Log of WR112

UT Date	Instrument	Mode	Filter
1998Jun05	NIRC	Aperture Masking: Annulus	ch4 (λ_0 2.269μm, $\Delta\lambda$ 0.155μm)
1998Sep30	NIRC	Aperture Masking: Annulus	K (λ_0 2.2135μm, $\Delta\lambda$ 0.427μm)
1999Apr26	NIRC	Aperture Masking: Annulus	K
1999Jul30	NIRC	Aperture Masking: Annulus	K
2000Jun24	NIRC	Aperture Masking: Annulus	K
2001Jun24	NIRC	Aperture Masking: Annulus	K
2002Jul24	NIRC	Aperture Masking: Annulus	K
2003May13	NIRC	Aperture Masking: Annulus	K
2004May29	NIRC	Aperture Masking: Annulus	H (λ_0 1.6575μm, $\Delta\lambda$ 0.333μm)
2004May29	NIRC	Aperture Masking: Annulus	K
2004Sep04	NIRC	Aperture Masking: Annulus	K
2020Aug18	NIRC2	Vortex Coronagraph	Lp (λ_0 3.776μm, $\Delta\lambda$ 0.700μm)

3.3. *Near-infrared imaging*

3.3.1. *Keck Aperture Masking*

WR 112 was observed eleven times between 1998 and 2004 at the Keck Observatory using the annulus aperture mask with the NIRC instrument (K. Matthews & B. T. Soifer 1994). The first discoveries of "pinwheel nebulae" were made using the Keck masking experiment (P. G. Tuthill et al. 1999; J. D. Monnier et al. 1999) and most of the Wolf-Rayet data has been published (J. D. Monnier et al. 2007). However, the full imaging of WR 112 has not appeared and here we present the full dataset for the first time.

Comprehensive explanations of the observing and imaging methodology for the Keck aperture masking experiment can be found in P. G. Tuthill et al. (2000), and we give only a short overview here. An annulus aperture mask is attached in front of the Keck-1 secondary mirror and a series of ∼100 short exposure frames are collected. The interference pattern can be analyzed using Fourier methods to extract the visibilities and closure phases for a range of baselines and closing triangles. These observables are calibrated using contemporaneous observations of calibrators. The pipeline produces OI-FITS data (T. A. Pauls et al. 2005) which can be used by a variety of image reconstruction packages, and here we used the MACIM algorithm (M. J. Ireland et al. 2006) for the images presented.

Table 4 contains the observing dates of the Keck aperture masking observations along with the observing filter used on each date. Note that most of the images were taken with an effective wavelength of ∼2.2μm. Figure 7 shows all the images in time order, revealing changes in the nebulosity and inner asymmetry over 6 years. Qualitatively, these images will constrain inner geometry in §4 when we connect the locations of the outer dust shells seen in the infrared with inner structure, along with the radio light curves which also constrains the innermost dust cone orientation over the orbit.

3.3.2. *Keck adaptive optics imaging*

L'-band (3.426-4.126 µm) observations of WR 112 were carried out with Keck/NIRC2 on UT2020Aug18 using the vortex coronagraph (E. Vargas Catalán et al. 2016; E. Serabyn et al. 2017). The observations employed the infrared pyramid wavefront sensor (C. Z. Bond et al. 2020), which operates at H-band, to control the Keck adaptive optics (AO) system. This was chosen due to heavy reddening of the target which precludes use of the Shack-Hartmann sensor which operates at R-band. The quadrant analysis of coronagraphic images for the tip-tilt sensing (QACITS; E. Huby et al. 2017) algorithm was used to keep the star aligned behind the mask by measuring tip/tilt residuals in the NIRC2 coronagraphic images and adjusting the tip/tilt offsets between the pyramid wavefront sensor and NIRC2. In total we obtained 87 frames, each consisting of 200 coadds of 0.053 s of the target with the central star being obscured by the vortex coronagraph. This results in a total integration time of 922 s on source. During the same night, we also observed five reference stars (HD162885, HD180732, HD181681, HD194479, HD194450) using the same vortex coronagraph setup. The only difference was that exposures consisting of 100 coadds of 0.18 s integrations were

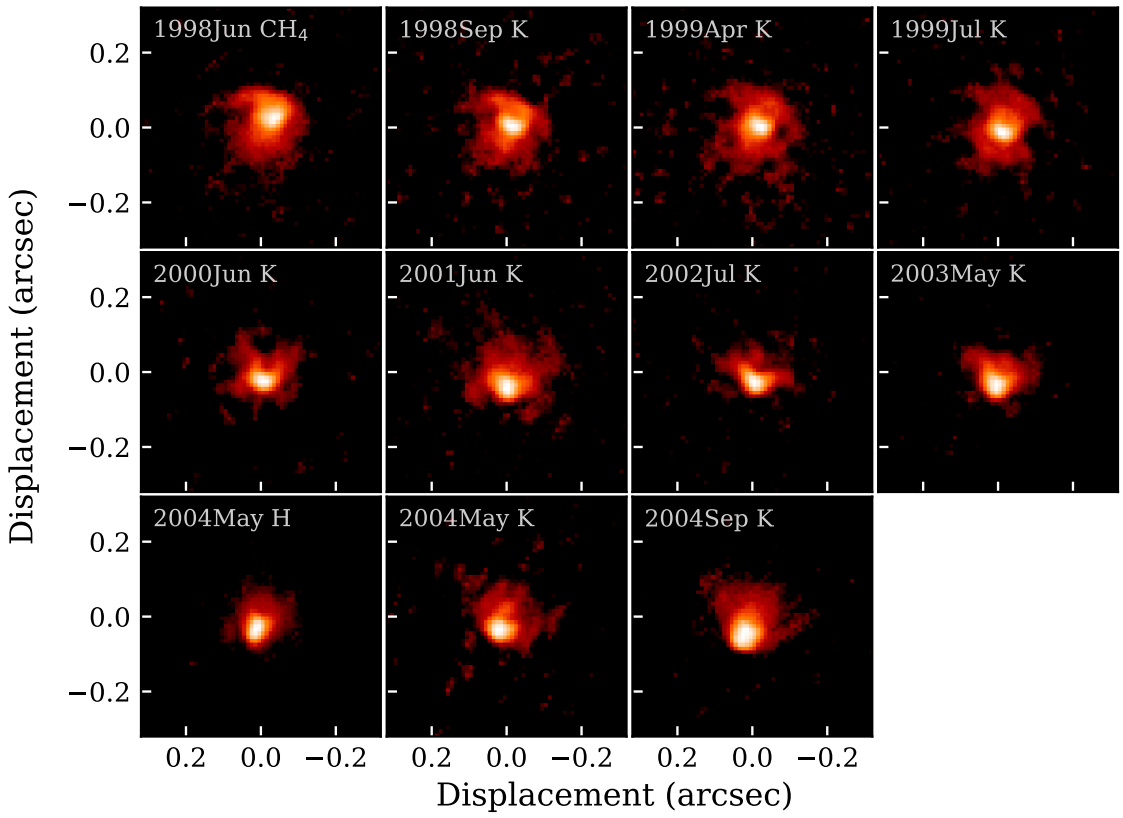

Figure 7. Here we see near-infrared images of the inner arcsecond of WR112 created using aperture masking interferometry on the Keck Telescope. The asymmetry near the center reveals the direction the dust cone is facing on each date and allows to make a connection between the outer dust shells observed in the mid-infrared and inner ones (see modeling in §4).

used. All of these images were compiled into the reference PSF library for the imaging analysis. Table 4 contains the observing log information.

Initial raw data processing was done with the vortex pre-processing pipeline (W. J. Xuan et al. 2018). This pipeline performs bad pixel correction, flat field division, background subtraction, and relative image registration. The star was assumed to be centered, on average across the observations, behind the coronagraphic mask (E. Huby et al. 2017). To remove the stellar point spread function (PSF), we tried both angular differential imaging (ADI; C. Marois et al. 2006) and reference star differential imaging (RDI). **With ADI, images of WR112 taken at other times (i.e., other parallactic angles where the dust has rotated in the observed sky plane) are used to build up a model of the stellar PSF. ADI enables us to use PSFs taken close in time with very similar AO performance, but the disk itself leaks into the stellar PSF model and can subtract itself. WIth RDI, images of the five reference stars are used to model and subtract the stellar PSF. RDI avoids disk self-subtraction but the stellar PSF model is less accurate as well.** In both cases, we use the KLIP implementation in the `pyKLIP` package for building up the model of the stellar diffraction pattern (J. J. Wang et al. 2015). For the ADI reductions, we built the KL modes across the entire frame, using any images of WR112 where the dust had rotated by at least 3 pixels due to ADI. For the RDI images, we also built the KL modes across the entire full frame, and used other vortex coronagraph images taken on the same night as reference images. We only use one KL mode to reconstruct the ADI and RDI images that appear in Figure 8.

The ADI image of WR112 shows the narrow limb brightened edge of the inner dust cone. This high resolution structure is very constraining for the wind models developed in §4. While ADI imaging can self-subtract nebulosity, we can see the presence of close-in emission (to the south of central source) in the RDI image also presented in Figure 8.

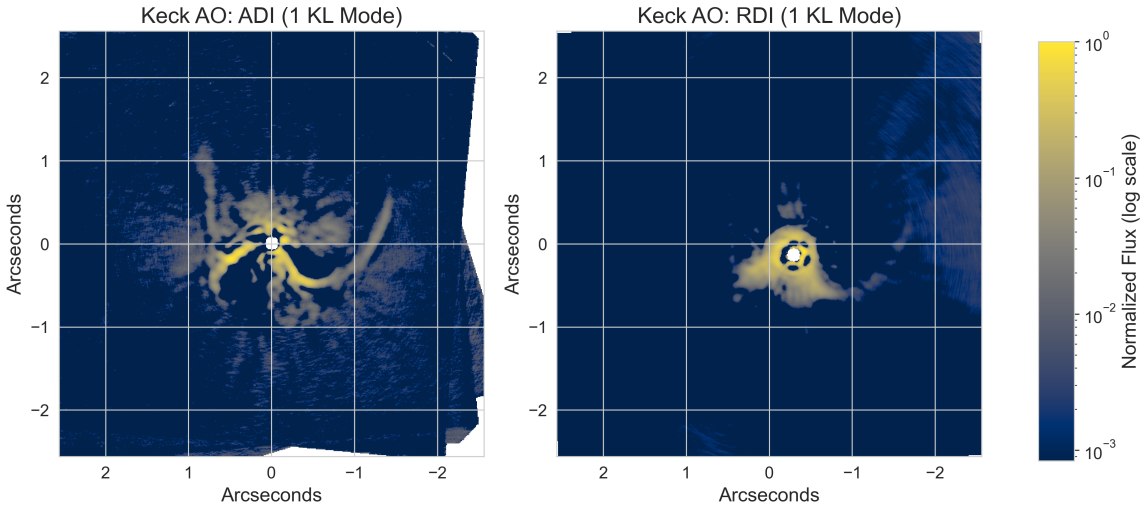

Figure 8. Keck adaptive optics imaging with the vortex coronagraph shows the edge of the dust cone beautifully. We present both the ADI and RDI images here and note that the central region is blocked by the coronagraph and is thus better revealed with Keck aperture masking images. The ADI reduction is more sensitive to sharp, faint features, while the RDI image better preserves the smooth, continuum features in the disk. We model the orientation and shape of this dust cone in §4.

4. EXTENDING THE COLLIDING-WIND MODEL

The diverse set of WR112 images is sensitive to dust structures over a range of radial regions from the binary. The near-IR aperture masking images (∼0.1 arcsec), near-IR AO images (∼1 arcsec) and mid-IR image (∼5 arcsec) together offer valuable constraints on the binary orbit and dust dynamics within the system, which we aim to leverage by fitting a geometric model that consistently explains the available observations.

4.1. *Model with circular orbit and uniform speed*

The underpinnings of the colliding-wind dust model (V. V. Usov 1991) was introduced in §2. Here we remind readers of the basics before we add additional complications, including orbital eccentricity and a wind-acceleration zone. We assume the column density distribution of the dust structure is produced on a cone-shaped wind-shock interface between the winds launched by the WR and O stars, after which the nucleated dust expands radially away from the binary along an imaginary conical surface. The orbital motion of the binary azimuthally offsets dust produced at one moment in time from the previous, resulting in a spiral dust surface in which all points expand radially away from the star. In addition to the binary's orbital elements, the model is also specified by the half-opening angle of the cone and the expansion speed of the dust. Models based on the same mechanism have been applied to describe the structure of WR 112 in the mid-IR (R. M. Lau et al. 2020) as well as in the context of other colliding-wind binaries such as WR140 (Y. Han et al. 2022; R. M. Lau et al. 2022), and Apep (J. R. Callingham et al. 2019; Y. Han et al. 2020; S. Bloot et al. 2022).

R. M. Lau et al. (2020) fitted a dust surface model to multiple mid-infrared images of WR 112, which revealed the motion of cool dust structures produced during approximately the three most recent orbital periods. We simulated the column density image of this model for the most recent orbital period of spiral dust structure. Compared to the mid-IR image, the near-IR AO image is sensitive to the high-resolution structure of much more close-in dust produced within the most recent orbital period. We find that the best-fit model parameters over-predict the size of this inner dust, but a delay in periastron passage by 0.3 orbits is able to simultaneously provide acceptable fits to both the AO and multi-epoch mid-IR images. We also simulated models of even closer-in dust structures at epochs that correspond to the aperture masking observations which are sensitive to the 0.1 arcsec scale, finding that this adjusted model reproduces the dust structures observed. We refer to this model with a circular orbit and uniform dust expansion speed as the "original model" and its parameters are displayed in Table 5. Note that the uncertainties were estimated by varying parameters independently and assessing the fit to the images by eye, rather than being quantified in a rigorous manner due to the lack of an effective metric (Y. Han et al. 2020).

Table 5. Parameters and plausibility of models invoked in this study. Additional parameters can be found in Table 1

	Original	Eccentric	Accelerating	Ecc. + Acc.
Eccentricity e	0	0.4	0	0.2
Argument of periastron ω [°]	0	290 ± 10	0	330 ± 20
Epoch of periastron T_0 [Jul. yr]	2021.0 ± 1.9	2019.1 ± 1.0	2012.3 ± 1.0	2010.7 ± 1.0
Dust expansion speed v [km s^{-1}]	1220 ± 60	$\mathbf{1290 \pm 80}$		
Initial velocity v_0 [km s^{-1}]			0	0
Terminal velocity v_d [km s^{-1}]			1360 ± 100	$\mathbf{1360 \pm 100}$
Acceleration phase [orbits]			1.10 ± 0.10	1.15 ± 0.10
Fits MIR geometry	Y	Y	Y	Y
Fits NIR AO geometry	Y	Y	Y	Y
Fits NIR masking geometry	Y	N	Y	Y
Fits radio light curve	N	N	Y	Y

In addition to the imaging data available, the radio light curve also constrains the orbit of the binary. At an almost edge-on viewing perspective, **the dominant stellar wind** along the line of the sight, which absorbs free-free emission from the shock interface, alternates between that of the O and WR stars. The much lower optical depth of the O star's wind results in periodic brightening of the radio flux density, the timing of which is determined by the orbital configuration. Such a constraint likely probes even closer to the binary, since the free-free absorption coefficient is approximately proportional to wind density squared, and therefore $1/r^4$, implying that only the most close-in regions to the binary contribute to the optical depth.

To test whether the geometric model is consistent with the observed radio light curve, we modelled the column density of the O star's wind assuming that it occupies the volume within the shock cone. More specifically, rather than simulating rings of dust that form on and expand along conical surfaces, **we simulated the stellar wind with concentric spherical caps**, each consisting of uniformly distributed particles, and are azimuthally offset from those produced earlier in time due to orbital motion. The corresponding WR wind model is obtained by subtracting the O star wind model from a spherical wind model computed with the same $1/r^4$ scaling.

Using such an approach, we find that the geometric model predicts the combined optical depth of the binary to dip, and therefore the radio flux to peak, from 2024 and 2028. However, the two epochs of radio observations imply that the radio flux should rise no earlier than 2015 and fall to quiescent levels no later than 2020. This implies that the geometric model differs from the observed radio peak by almost half an orbital period.

Indeed, such a discrepancy might be expected based on an intuitive picture of the orbit of WR 112. At mild eccentricities and for nearly edge-on orbits, the orbital phase at which the O star's stellar wind cone sweeps across the line of sight is primarily affected by ω and T_0 (and not by Ω). Specifically, a near-transit (with the O star in front) of the two stars is achieved approximately a quarter of an orbit after T_0 for a circular orbit or with an offset based on the argument of periastron ω for an eccentric orbit. We therefore expect the radio peak to occur at approximately

$$T_\mathrm{bright} \approx T_0 + P/4 - \frac{\omega}{360^\circ} P. \tag{1}$$

For this circular orbit model, we therefore expect the radio peak to be centred at approximately 2026, which the wind modelling confirms. In order for the radio peak to be consistent with the observations, we therefore require $T_0 - (\omega/360^\circ)P$ to be approximately between 2012 and 2013. A mechanism that alters the geometry of the spiral is therefore required to simultaneously explain all observations.

4.2. *Eccentric model*

Mild orbital eccentricity is able to warp the spiral geometry, as is understood to be the case in WR140 (P. M. Williams et al. 2009; Y. Han et al. 2022), potentially allowing for a simultaneous fit to the imaging observations and radio flux. However, we experimented with a range of model parameters and found no combination that could explain all four of the AO, masking, mid-IR and radio constraints simultaneously.

Eccentricity distorts the shape of the dust spiral in different ways at different points along the orbit, which implies that ω cannot be fixed at 0 as in the case of the original model. Simultaneously varying ω and T_0, we found that an

eccentricity as high as 0.4 is still able to offer a close fit to the near-IR geometry while simultaneously reproducing the location of the mid-IR structures with the parameters listed in Table 5. However, such a model cannot reproduce the masking geometry, displaying a discrepancy much like a phase offset, reflecting that the warping introduced by eccentricity is inconsistent with the kind of warping suggested by the data. Furthermore, the predicted radio peak time from wind models that we correspondingly simulated predict radio brightening from 2024 to 2028, which is significantly different from the observations. An alternative mechanism to warp the basic spiral geometry is therefore required.

4.3. *Accelerating model*

An expected process that is able to warp the close-in geometry and potentially explain these observations is a non-uniform expansion speed of dust. Acceleration of dust due to radiation pressure is expected to be important given the intense radiation field of the binary ($4{\times}10^5\,L_\odot$; A. A. C. Sander et al. 2019), and observational evidence for such an acceleration has been suggested in the context of WR140 (Y. Han et al. 2022). **Assuming the same 19.4 yr orbital period (R. M. Lau et al. 2020),** we modelled the variable expansion speed of dust to consist of two phases following its nucleation site assumed to be at the binary: a constant acceleration phase starting from a **post-shock** velocity of v_0 and reaching a velocity of v_d after an orbital phase of $\Delta\phi_a$, followed by expansion at a constant speed of v_d.

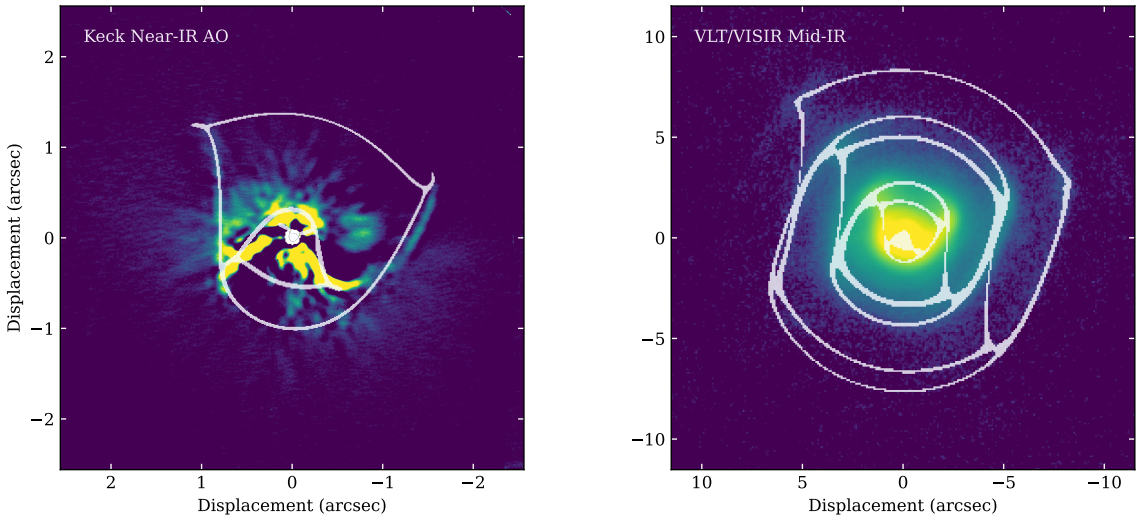

Figure 9. Comparison of accelerating colliding-wind model prediction to the Keck near-infrared adaptive optics image and the VLT/VISIR mid-infrared image (R. M. Lau et al. 2022). The model outline is shown with white lines, which are overlaid on the data. Visualizations of the model are provided in Figure 12.

Motivated by Eq. 1, we set the periastron passage time at 2012.3 to be consistent with expectations from the epoch of radio brightening while setting e to be 0. With i, Ω, P and θ_w largely fixed by the multiple epochs of further out mid-IR geometry, the only free parameters are those defining the acceleration curve. We find that for the post-shock material that starts accelerating from a standstill ($v_0 = 0$), accelerating to 1360 km s^{-1} over approximately one orbit is able to simultaneously reproduce the mid-IR, AO and masking geometry. **Terminal velocity is reached at a radius of approximately 3100 au or 0.94″.** Comparisons of the AO and mid-IR geometry between the accelerating model and the observations are shown in Figure 9. The masking model images along with a direct comparison to the Keck masking images are shown in Figure 10. Furthermore, radio light curve modelling using our wind model does indeed produce brightening that is broadly consistent with the radio flux observations, as shown in Figure 11. The best-fit model parameters are included in Table 5. We also present visualizations of the model for a few different viewing perspectives in Figure 12.

Note that as the radio flux observations contain flux contributions (such as wind emission, which could contribute flux throughout the orbit) not accounted for in our model, a direct comparison of the absolute values predicted is unimportant for our purposes, which focuses on comparing the peak epoch of radio flux. **We therefore calculated the radio light curve from the model as displayed in Figure 11. We assumed that the radio flux**

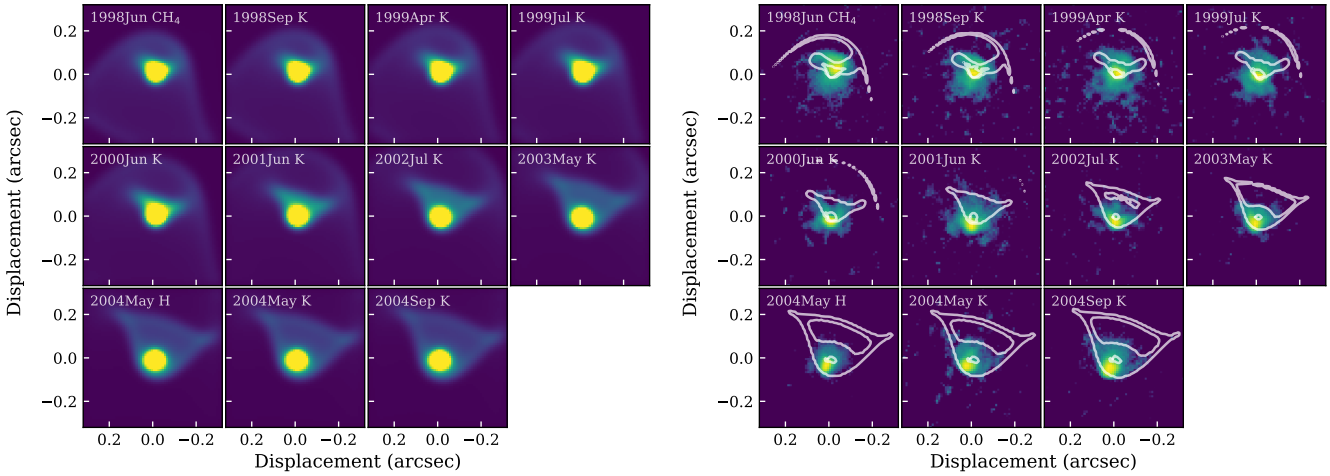

Figure 10. Here we see model predictions (left panel) of the inner arcsecond dust emission from the accelerating wind model for each Keck masking dataset, along with original Keck masking images overlaid with white contours of the corresponding models (right panel). Models were convolved with K-band diffraction-limited point spread functions.

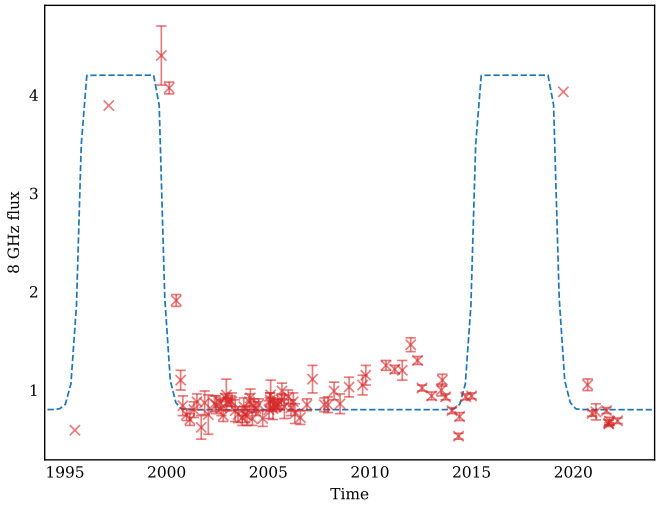

Figure 11. The figure shows the observed radio flux measurements (red crosses) overlaid with the radio model (dashed blue line) that incorporates wind acceleration, as described in §4.3. We roughly reproduce the start and stop times of the radio-bright phase while maintaining fits to the dust shell locations observed in the infrared. Note our simple model does not explain the mysterious rise and decline in flux around 2012.

is modulated by the optical depth of the free-free emission along the line of sight to the embedded non-thermal source, given by

$$F_{\rm radio}(t) \propto \exp\left[-(\tau_{\rm O}(t) + \tau_{\rm WR}(t))\right], \tag{2}$$

where $\tau_{\rm O}$ and $\tau_{\rm WR}$ are the optical depth of the O and WR winds to free-free emission at the colliding-wind region, temporal variations of which are predicted by the wind column density model developed here. Note that the model only constrains $\tau_{\rm O}$ and $\tau_{\rm WR}$ in proportional terms and we do not constrain the wind densities directly here. Based on the radio spectral indices we are confident the WR wind is optically-thick and likewise that the O-star wind is optically-thin or not much above unity (see deeper discussion by J. D. Monnier et al. 2002). We therefore focus on modeling the trends in the radio flux over time rather than its physical flux value, and $F_{\rm radio}(t)$ is linearly transformed to fit the flux values of the observations. This model is able to reproduce the switch in state between the radio maximum and minimum over an orbital period. Interestingly, a secondary brightening (2008 to 2013) is also observed but not predicted by the

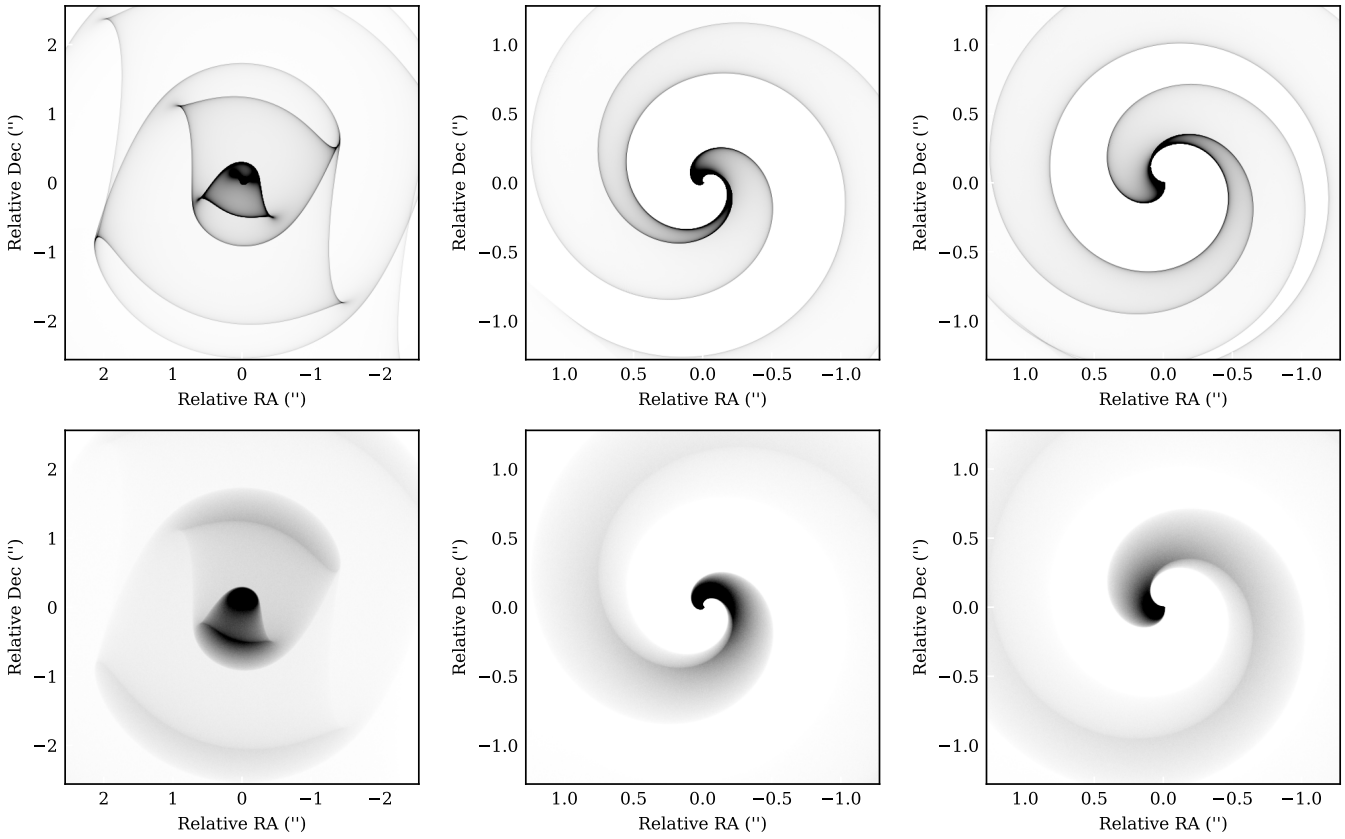

Figure 12. Visualization of the WR 112 models simulated at the epoch of the near-IR AO observations. Top row: dust column density models. Bottom row: O star wind column density models. Left column: accelerating model of WR 112 as viewed from Earth. Middle column: face-on view of the accelerating model (setting the observer at the left of the frame looking right). Right column: face-on models simulated without acceleration to visualize its effects by comparison with the middle column (observer at the left of the frame looking right)

model, the nature of which will require further work to investigate given that its flux measurements presented here were obtained at only one frequency.

While we assumed a circular orbit in this model, it is possible that the orbit of the binary is mildly eccentric. We experimented with the effect of incorporating a **nonzero** eccentricity into the dust and wind models, finding that a model largely consistent with all imaging and radio flux constraints could be achieved with the parameters under the "eccentric + accelerating" model in Table 5. While our accelerating models assume **a post-shock velocity of** $v_0 = 0$, dust is unlikely to form at a standstill, which is achieved only at the apex of the shock cone between the two stellar winds, but rather at tens to ∼100 au downstream (P. G. Tuthill et al. 2008; P. M. Williams et al. 2009) following sufficient cooling. However, the phase of the binary, which is largely fixed by the radio light curve, implies that the geometry of the spiral as seen in the near-IR AO image (Figure 8) rapidly coils towards and disappears into the star when approaching the center. This geometry can only be reproduced with a v_0 that is significantly smaller than the terminal wind speed. We therefore set v_0 to 0 our model for simplicity. The conditions on the orbital phase imposed by the radio light curve can be partially relaxed with the introduction of a nonzero eccentricity, however we did not find any combination of orbital parameters that could simultaneously reproduce the imaging and radio light curve even if v_0 was set to only one third of the terminal wind speed. It is important to recognize that while the model aims to describe the dust geometry, what it fundamentally models is the dynamical evolution of material both before and after nucleating into dust. It is possible that this acceleration from a low initial velocity reflects the motion of material starting from post-shock wind near the apex of the shock cone before nucleating into dust. JWST observations (N. D. Richardson et al. 2025) may be able to offer sufficiently sharp resolution and high sensitivity to better constrain the

eccentricity of the binary based on the geometry of further out dust shells in the mid-IR and its implications on the motion of post-shock wind and dust.

4.4. *Comparison with WR 140*

The successful reproduction of available imaging and radio flux constraints in the accelerating model(s) for WR112 provides observational evidence of dust acceleration in a second WR binary after WR 140. The two systems make for an interesting comparison.

In the model for WR 140 by Y. Han et al. (2022), dust accelerates from approximately 1800 to 2500 km s^{-1} over approximately 2 yr, during which it travelled approximately 1,000 au from the binary. Here in WR 112, **acceleration** from approximately 0 to 1400 km s^{-1} occurs over 21 yr, or 6,000 au from the binary. Since radiation pressure is proportional to stellar luminosity, which is approximately 4 times stronger in WR 140 ($1.43\times10^6\,L_\odot$) compared to WR 112 ($4\times10^5\,L_\odot$), the 5 times faster acceleration in WR 140 compared to WR 112 may therefore be largely consistent with differences in stellar luminosity.

It is worth noting that key differences exist in the observations and modelling of the two systems. Whereas the acceleration parameters for WR 112 from this study were primarily set by a single epoch of near-IR AO geometry in combination with orbital constraints from radio flux variations and the large-scale dust structure in the mid-IR, the orbit of WR 140 is tightly constrained from relative astrometry and the acceleration was measured by cross-correlating features across a set of multi-epoch images which together track the expansion of each feature over time. Furthermore, the measured displacement-time diagram for WR 140 was parameterized and fitted with a three-phase model, which included an earlier constant speed outflow phase before acceleration begins. In contrast, a model with reduced complexity was implemented for WR 112 given the lack of a well-sampled displacement-time diagram shortly following dust production, which still offers the flexibility to model the shape of features in the near-IR AO image. Future work that better tracks the expansion of dust close to the binary will help provide more robust constraints on the dynamics of dust following their formation.

5. CONCLUSIONS

We have presented extensive new datasets for WR 112, including new X-ray, radio, aperture masking, and adaptive optics imaging. This dust-producing colliding wind binary is in an unusually long orbit and viewed close to edge-on. After a long period in a low-state, the radio flux recently increased then returned to quiescent levels, suggesting an orbital period of 20.0±0.1 yrs. With multi-epoch imaging at different scales, we show that a simple uniform-outflow model can not fit the full dataset. However, we do find that accelerating wind models fit the imaging and radio data although we do not constrain well the eccentricity nor the exact form of the acceleration flow in this work.

While our geometrical models produce good qualitative fits to our diverse dataset, the parameters we present are not unique and still depend on a number of model assumptions. That said, our model is a major step forward in understanding WR 112 and will guide full hydrodynamical modeling and radiative transfer calculations to further constrain the physics of colliding wind binaries. With a self-consistent physical model we can link the radio and X-ray properties to learn how high-temperature plasmas cool in these violent shocked flows between two massive stellar winds. We add WR 112 to a small – but growing – list of colliding wind systems with sufficiently well-known properties suitable for detailed numerical modelling. **Future work may wish to further explore post-shock kinematics and the cause of the secondary brightening of the radio light curve.**

Facilities: Keck:I (NIRC), Keck:II (NIRC2), VLA, EVLA, ATCA, CXO, Swift

Software: astropy (Astropy Collaboration et al. 2013, 2018, 2022)

APPENDIX

A. RADIO PHOTOMETRY

Here we include Table 6 which contains the full radio photometry dataset used in this paper, including every known measurement in the literature. When WR 112 was not detected, a 2-σ upper limit is reported.

Table 6. Radio Observations of WR112 (upper-limits are 2-σ)

UT Date	Facility	λ (cm)	ν (GHz)	F_ν (mJy)	Reference
1995Jun27	ATCA	3.0	10.0	0.68 ± 0.13	C. Leitherer et al. (1997)
1995Jun27	ATCA	6.0	5.0	< 0.26	C. Leitherer et al. (1997)
1997Feb25	ATCA	13.0	2.3	3.80 ± 0.16	J. M. Chapman et al. (1999)
1997Feb25	ATCA	20.0	1.5	< 0.74	J. M. Chapman et al. (1999)
1999Sep27	VLA	1.3	23.1	4.05 ± 0.25	J. D. Monnier et al. (2002)
1999Sep27	VLA	2.0	15.0	4.20 ± 0.30	J. D. Monnier et al. (2002)
1999Sep27	VLA	3.6	8.3	4.40 ± 0.30	J. D. Monnier et al. (2002)
1999Sep27	VLA	6.2	4.8	4.12 ± 0.10	J. D. Monnier et al. (2002)
1999Sep27	VLA	20.0	1.5	2.71 ± 0.17	J. D. Monnier et al. (2002)
2000Feb15	VLA	1.3	23.1	3.97 ± 0.12	J. D. Monnier et al. (2002)
2000Feb15	VLA	2.0	15.0	4.39 ± 0.17	J. D. Monnier et al. (2002)
2000Feb15	VLA	3.6	8.3	4.07 ± 0.06	J. D. Monnier et al. (2002)
2000Feb15	VLA	6.2	4.8	3.75 ± 0.08	J. D. Monnier et al. (2002)
2000Feb15	VLA	20.0	1.5	2.30 ± 0.30	J. D. Monnier et al. (2002)
2000Jun20	VLA	2.0	15.0	1.87 ± 0.16	this work
2000Jun20	VLA	3.6	8.3	1.91 ± 0.06	this work
2000Jun20	VLA	6.2	4.8	1.55 ± 0.08	this work
2000Jun20	VLA	20.0	1.5	1.00 ± 0.20	this work
2000Sep08	VLA	2.0	15.0	1.28 ± 0.13	this work
2000Sep08	VLA	3.6	8.3	1.10 ± 0.10	this work
2000Sep08	VLA	6.2	4.8	0.90 ± 0.08	this work
2000Sep08	VLA	20.0	1.5	< 0.90	this work
2000Oct17	VLA	2.0	15.0	1.02 ± 0.17	this work
2000Oct17	VLA	3.6	8.3	0.84 ± 0.10	this work
2000Oct17	VLA	6.2	4.8	0.68 ± 0.07	this work
2000Oct17	VLA	20.0	1.5	0.55 ± 0.15	this work
2000Dec23	VLA	0.7	42.9	< 1.20	this work
2000Dec23	VLA	2.0	15.0	0.76 ± 0.11	this work
2000Dec23	VLA	3.6	8.3	0.75 ± 0.06	this work
2000Dec23	VLA	6.2	4.8	0.60 ± 0.10	this work
2001Feb21	VLA	2.0	15.0	1.30 ± 0.20	this work
2001Feb21	VLA	3.6	8.3	0.70 ± 0.06	this work
2001Feb21	VLA	6.2	4.8	0.56 ± 0.06	this work
2001Feb21	VLA	20.0	1.5	0.33 ± 0.10	this work
2001May04	VLA	2.0	15.0	1.30 ± 0.30	this work
2001May04	VLA	3.6	8.3	0.80 ± 0.08	this work
2001May04	VLA	6.2	4.8	0.45 ± 0.05	this work
2001May04	VLA	20.0	1.5	0.34 ± 0.11	this work
2001Jun28	VLA	2.0	15.0	1.25 ± 0.18	this work
2001Jun28	VLA	3.6	8.3	0.88 ± 0.08	this work

Table 6 *continued on next page*

Table 6 *(continued)*

UT Date	Facility	λ (cm)	ν (GHz)	F_ν (mJy)	Reference
2001Jun28	VLA	6.2	4.8	0.70 ± 0.15	this work
2001Jun28	VLA	20.0	1.5	0.50 ± 0.18	this work
2001Sep13	VLA	2.0	15.0	1.35 ± 0.25	this work
2001Sep13	VLA	3.6	8.3	0.62 ± 0.12	this work
2001Sep13	VLA	6.2	4.8	0.58 ± 0.10	this work
2001Sep13	VLA	20.0	1.5	< 0.82	this work
2001Nov13	VLA	2.0	15.0	1.35 ± 0.25	this work
2001Nov13	VLA	3.6	8.3	0.87 ± 0.12	this work
2001Nov13	VLA	6.2	4.8	0.61 ± 0.07	this work
2001Nov13	VLA	20.0	1.5	< 0.82	this work
2002Jan18	VLA	3.6	8.3	0.75 ± 0.20	this work
2002May07	VLA	3.6	8.3	0.86 ± 0.08	this work
2002Jun06	VLA	3.6	8.3	0.85 ± 0.09	this work
2002Jun06	VLA	20.0	1.5	< 0.28	this work
2002Aug17	VLA	3.6	8.3	0.87 ± 0.05	this work
2002Aug17	VLA	20.0	1.5	< 0.13	this work
2002Sep11	VLA	3.6	8.3	0.82 ± 0.08	this work
2002Oct14	VLA	3.6	8.3	0.74 ± 0.06	this work
2002Oct14	VLA	20.0	1.5	< 0.39	this work
2002Nov22	VLA	3.6	8.3	0.92 ± 0.04	this work
2002Nov22	VLA	20.0	1.5	< 0.64	this work
2002Dec08	VLA	3.6	8.3	0.95 ± 0.16	this work
2002Dec08	VLA	20.0	1.5	< 0.50	this work
2003Jan05	VLA	3.6	8.3	0.88 ± 0.04	this work
2003Feb22	VLA	3.6	8.3	0.89 ± 0.06	this work
2003Mar17	VLA	3.6	8.3	0.88 ± 0.09	this work
2003May15	VLA	2.0	15.0	1.90 ± 0.56	this work
2003May15	VLA	3.6	8.3	0.79 ± 0.11	this work
2003Jul06	VLA	3.6	8.3	0.75 ± 0.08	this work
2003Jul06	VLA	20.0	1.5	< 0.40	this work
2003Sep19	VLA	3.6	8.3	0.72 ± 0.08	this work
2003Sep19	VLA	20.0	1.5	< 0.33	this work
2003Oct17	VLA	3.6	8.3	0.83 ± 0.09	this work
2003Oct17	VLA	20.0	1.5	< 0.36	this work
2003Nov10	VLA	3.6	8.3	0.75 ± 0.08	this work
2003Dec14	VLA	3.6	8.3	0.74 ± 0.10	this work
2003Dec14	VLA	6.2	4.8	0.50 ± 0.10	this work
2004Jan26	VLA	3.6	8.3	0.88 ± 0.08	this work
2004Jan26	VLA	20.0	1.5	< 0.62	this work
2004Feb13	VLA	3.6	8.3	0.92 ± 0.09	this work
2004Mar20	VLA	3.6	8.3	0.71 ± 0.07	this work

Table 6 *continued on next page*

Table 6 *(continued)*

UT Date	Facility	λ (cm)	ν (GHz)	F_ν (mJy)	Reference
2004Apr16	VLA	3.6	8.3	0.84 ± 0.07	this work
2004Apr16	VLA	20.0	1.5	< 0.51	this work
2004May22	VLA	3.6	8.3	0.81 ± 0.07	this work
2004May22	VLA	20.0	1.5	< 0.35	this work
2004Jul12	VLA	3.6	8.3	0.85 ± 0.06	this work
2004Jul12	VLA	20.0	1.5	< 1.40	this work
2004Sep21	VLA	3.6	8.3	0.71 ± 0.08	this work
2004Sep21	VLA	20.0	1.5	< 0.26	this work
2005Jan12	VLA	3.6	8.3	0.80 ± 0.09	this work
2005Jan12	VLA	20.0	1.5	0.51 ± 0.16	this work
2005Jan30	VLA	3.6	8.3	0.88 ± 0.09	this work
2005Jan30	VLA	20.0	1.5	< 0.28	this work
2005Feb03	VLA	3.6	8.3	0.90 ± 0.07	this work
2005Feb11	VLA	3.6	8.3	0.95 ± 0.15	this work
2005Mar05	VLA	20.0	1.5	0.54 ± 0.23	this work
2005Mar24	VLA	3.6	8.3	0.81 ± 0.11	this work
2005Apr16	VLA	3.6	8.3	0.86 ± 0.05	this work
2005May20	VLA	3.6	8.3	0.83 ± 0.05	this work
2005Jun06	VLA	3.6	8.3	0.85 ± 0.05	this work
2005Jul04	VLA	3.6	8.3	0.85 ± 0.05	this work
2005Jul04	VLA	20.0	1.5	< 0.32	this work
2005Aug22	VLA	3.6	8.3	0.90 ± 0.06	this work
2005Aug22	VLA	20.0	1.5	< 0.74	this work
2005Sep02	VLA	3.6	8.3	0.99 ± 0.08	this work
2005Sep02	VLA	20.0	1.5	< 0.70	this work
2005Oct16	VLA	3.6	8.3	0.83 ± 0.12	this work
2005Dec24	VLA	3.6	8.3	0.93 ± 0.07	this work
2005Dec24	VLA	20.0	1.5	< 4.00	this work
2006Feb11	VLA	3.6	8.3	0.82 ± 0.08	this work
2006Feb11	VLA	20.0	1.5	< 0.26	this work
2006Mar25	VLA	3.6	8.3	0.88 ± 0.09	this work
2006Mar25	VLA	20.0	1.5	< 0.38	this work
2006Apr22	VLA	3.6	8.3	0.76 ± 0.10	this work
2006Apr22	VLA	20.0	1.5	< 0.58	this work
2006Jul30	VLA	3.6	8.3	0.72 ± 0.07	this work
2006Jul30	VLA	20.0	1.5	< 0.40	this work
2006Nov25	VLA	3.6	8.3	0.85 ± 0.06	this work
2006Nov25	VLA	20.0	1.5	< 1.20	this work
2007Mar05	VLA	3.6	8.3	1.11 ± 0.14	this work
2007Oct03	VLA	3.6	8.3	0.85 ± 0.07	this work
2007Dec09	VLA	3.6	8.3	0.85 ± 0.08	this work

Table 6 *continued on next page*

Table 6 *(continued)*

UT Date	Facility	λ (cm)	ν (GHz)	F_ν (mJy)	Reference
2008Mar26	VLA	3.6	8.3	0.99 ± 0.09	this work
2008Jul12	VLA	3.6	8.3	0.86 ± 0.10	this work
2008Dec21	VLA	3.6	8.3	1.03 ± 0.10	this work
2009Aug21	VLA	3.6	8.3	1.05 ± 0.10	this work
2009Oct17	VLA	3.6	8.3	1.15 ± 0.10	this work
2010Oct15	VLA	3.6	8.3	1.25 ± 0.05	this work
2011Mar22	VLA	3.6	8.3	1.21 ± 0.04	this work
2011Aug03	VLA	3.6	8.3	1.20 ± 0.10	this work
2012Jan02	VLA	3.6	8.3	1.46 ± 0.07	this work
2012May04	VLA	3.6	8.3	1.30 ± 0.04	this work
2012Jul23	VLA	3.6	8.3	1.02 ± 0.03	this work
2013Jan12	VLA	3.6	8.3	0.94 ± 0.04	this work
2013Jul05	VLA	3.6	8.3	1.00 ± 0.06	this work
2013Jul23	VLA	3.6	8.3	1.10 ± 0.06	this work
2013Sep20	VLA	3.6	8.3	0.93 ± 0.03	this work
2014Jan13	VLA	3.6	8.3	0.79 ± 0.03	this work
2014May11	VLA	3.6	8.3	0.53 ± 0.03	this work
2014May29	VLA	3.6	8.3	0.73 ± 0.04	this work
2014Sep18	VLA	3.6	8.3	0.93 ± 0.03	this work
2014Dec31	VLA	3.6	8.3	0.94 ± 0.03	this work
2019Jul06	VLASS	10.0	3.0	4.00 ± 0.50	Y. A. Gordon et al. (2021)
2020Sep15	ATCA	1.4	21.2	1.45 ± 0.10	this work
2020Sep15	ATCA	1.8	16.7	1.33 ± 0.08	this work
2020Sep15	ATCA	3.3	9.0	1.05 ± 0.06	this work
2020Sep15	ATCA	5.5	5.5	0.93 ± 0.12	this work
2020Dec04	VLA	1.2	25.0	1.22 ± 0.06	this work
2020Dec04	VLA	1.3	23.0	1.17 ± 0.07	this work
2020Dec04	VLA	1.4	21.0	1.27 ± 0.06	this work
2020Dec04	VLA	1.6	19.0	1.09 ± 0.05	this work
2020Dec04	VLA	1.8	17.0	1.08 ± 0.07	this work
2020Dec04	VLA	2.0	15.0	0.93 ± 0.03	this work
2020Dec04	VLA	2.3	13.0	0.97 ± 0.03	this work
2020Dec04	VLA	2.7	11.0	0.83 ± 0.03	this work
2020Dec04	VLA	3.3	9.0	0.76 ± 0.03	this work
2020Dec04	VLA	4.3	7.0	0.60 ± 0.03	this work
2020Dec04	VLA	6.0	5.0	0.62 ± 0.03	this work
2020Dec04	VLA	20.0	1.5	0.19 ± 0.05	this work
2021Feb11	ATCA	1.4	21.2	1.35 ± 0.10	this work
2021Feb11	ATCA	1.8	16.7	1.23 ± 0.08	this work
2021Feb11	ATCA	3.3	9.0	0.78 ± 0.08	this work
2021Feb11	ATCA	5.5	5.5	0.70 ± 0.15	this work

Table 6 *continued on next page*

Table 6 *(continued)*

UT Date	Facility	λ (cm)	ν (GHz)	F_ν (mJy)	Reference
2021Aug20	VLA	1.2	25.0	1.32 ± 0.05	this work
2021Aug20	VLA	1.3	23.0	1.27 ± 0.05	this work
2021Aug20	VLA	1.4	21.0	1.29 ± 0.05	this work
2021Aug20	VLA	1.6	19.0	1.20 ± 0.03	this work
2021Aug20	VLA	1.8	17.0	1.04 ± 0.04	this work
2021Aug20	VLA	2.0	15.0	1.06 ± 0.03	this work
2021Aug20	VLA	2.3	13.0	0.94 ± 0.03	this work
2021Aug20	VLA	2.7	11.0	0.87 ± 0.03	this work
2021Aug20	VLA	3.3	9.0	0.79 ± 0.03	this work
2021Aug20	VLA	4.3	7.0	0.65 ± 0.03	this work
2021Aug20	VLA	6.0	5.0	0.52 ± 0.04	this work
2021Sep24	VLA	2.7	11.0	0.70 ± 0.03	this work
2021Sep24	VLA	3.3	9.0	0.66 ± 0.03	this work
2021Oct03	ATCA	1.4	21.2	0.98 ± 0.04	this work
2021Oct03	ATCA	1.8	16.7	0.96 ± 0.02	this work
2021Oct03	ATCA	3.3	9.0	0.66 ± 0.01	this work
2021Oct03	ATCA	5.5	5.5	0.58 ± 0.02	this work
2021Oct11	VLA	2.7	11.0	0.80 ± 0.04	this work
2021Oct11	VLA	3.3	9.0	0.69 ± 0.04	this work
2022Mar06	ATCA	1.4	21.2	0.94 ± 0.22	this work
2022Mar06	ATCA	1.8	16.7	1.12 ± 0.12	this work
2022Mar06	ATCA	3.3	9.0	0.69 ± 0.03	this work
2022Mar06	ATCA	5.5	5.5	0.53 ± 0.03	this work

ACKNOWLEDGMENTS

The authors would like to thank a few colleagues who have contributed to obtaining this data presented herein: Anthony Pollack, Andreas Sander, and David Espinoza. We also thank the anonymous referee for their help in improving the manuscript.

Support for this work was provided by the National Aeronautics and Space Administration through Chandra Award Number 23200246 issued by the Chandra X-ray Center, which is operated by the Smithsonian Astrophysical Observatory for and on behalf of the National Aeronautics Space Administration under contract NAS8-03060.

The National Radio Astronomy Observatory is a facility of the National Science Foundation operated under cooperative agreement by Associated Universities, Inc.

The Australia Telescope Compact Array is part of the Australia Telescope National Facility (grid.421683.a) which is funded by the Australian Government for operation as a National Facility managed by CSIRO. We acknowledge the Gomeroi people as the traditional owners of the Observatory site.

Some of the data presented herein were obtained at Keck Observatory, which is a private 501(c)3 non-profit organization operated as a scientific partnership among the California Institute of Technology, the University of California, and the National Aeronautics and Space Administration. The Observatory was made possible by the generous financial support of the W. M. Keck Foundation. The authors wish to recognize and acknowledge the very significant cultural role and reverence that the summit of Maunakea has always had within the Native Hawaiian community. We are most fortunate to have the opportunity to conduct observations from this mountain.

M.F.C. and K.H. are supported by NASA under award numbers 80GSFC21M0002 and 80GSFC24M0006. J.J.W. acknowledges support by the Heising-Simons Foundation (#2023-4598) and the Alfred P. Sloan Foundation. S.B. acknowledges funding from the Dutch research council (NWO) under the talent programme (Vidi grant VI.Vidi.203.093). J.D.M. and M.C. acknowledge support from Chandra Award No. GO2-23012B. JRC acknowledges funding from the European Union via the European Research Council (ERC) grant Epaphus (project number: 101166008). CMPR acknowledges support from NASA Chandra Theory grant number TM3-24001X.

REFERENCES

Arnaud, K. A. 1996, in Astronomical Society of the Pacific Conference Series, Vol. 101, Astronomical Data Analysis Software and Systems V, ed. G. H. Jacoby & J. Barnes, 17

Astropy Collaboration, Robitaille, T. P., Tollerud, E. J., et al. 2013, A&A, 558, A33, doi: 10.1051/0004-6361/201322068

Astropy Collaboration, Price-Whelan, A. M., Sipőcz, B. M., et al. 2018, AJ, 156, 123, doi: 10.3847/1538-3881/aabc4f

Astropy Collaboration, Price-Whelan, A. M., Lim, P. L., et al. 2022, ApJ, 935, 167, doi: 10.3847/1538-4357/ac7c74

Bloot, S., Callingham, J. R., & Marcote, B. 2022, MNRAS, 509, 475, doi: 10.1093/mnras/stab2976

Bond, C. Z., Cetre, S., Lilley, S., et al. 2020, Journal of Astronomical Telescopes, Instruments, and Systems, 6, 039003, doi: 10.1117/1.JATIS.6.3.039003

Callingham, J. R., Tuthill, P. G., Pope, B. J. S., et al. 2019, Nature Astronomy, 3, 82, doi: 10.1038/s41550-018-0617-7

CASA Team, Bean, B., Bhatnagar, S., et al. 2022, PASP, 134, 114501, doi: 10.1088/1538-3873/ac9642

Cash, W. 1979, ApJ, 228, 939, doi: 10.1086/156922

Chapman, J. M., Leitherer, C., Koribalski, B., Bouter, R., & Storey, M. 1999, ApJ, 518, 890, doi: 10.1086/307314

Cohen, M., & Vogel, S. N. 1978, MNRAS, 185, 47. http://adsabs.harvard.edu/cgi-bin/nph-bib_query?bibcode=1978MNRAS.185...47C&db_key=AST

David-Uraz, A., Moffat, A. F. J., Chené, A.-N., et al. 2012, MNRAS, 426, 1720, doi: 10.1111/j.1365-2966.2012.21736.x

Fruscione, A., McDowell, J. C., Allen, G. E., et al. 2006, in Society of Photo-Optical Instrumentation Engineers (SPIE) Conference Series, Vol. 6270, Observatory Operations: Strategies, Processes, and Systems, ed. D. R. Silva & R. E. Doxsey, 62701V, doi: 10.1117/12.671760

Gordon, Y. A., Boyce, M. M., O'Dea, C. P., et al. 2021, ApJS, 255, 30, doi: 10.3847/1538-4365/ac05c0

Hamaguchi, K., Corcoran, M. F., Pittard, J. M., et al. 2018, Nature Astronomy, 2, 731, doi: 10.1038/s41550-018-0505-1

Han, Y., Tuthill, P. G., Lau, R. M., & Soulain, A. 2022, Nature, 610, 269, doi: 10.1038/s41586-022-05155-5

Han, Y., Tuthill, P. G., Lau, R. M., et al. 2020, MNRAS, 498, 5604, doi: 10.1093/mnras/staa2349

Huby, E., Bottom, M., Femenia, B., et al. 2017, A&A, 600, A46, doi: 10.1051/0004-6361/201630232

Ireland, M. J., Monnier, J. D., & Thureau, N. 2006, in Society of Photo-Optical Instrumentation Engineers (SPIE) Conference Series, Vol. 6268, Advances in Stellar Interferometry, ed. J. D. Monnier, M. Schöller, & W. C. Danchi, 62681T, doi: 10.1117/12.670940

Kaastra, J. S., & Bleeker, J. A. M. 2016, A&A, 587, A151, doi: 10.1051/0004-6361/201527395

Lau, R. M., Hankins, M. J., Han, Y., et al. 2020, ApJ, 900, 190, doi: 10.3847/1538-4357/abaab8

Lau, R. M., Hankins, M. J., Han, Y., et al. 2022, Nature Astronomy, 6, 1308, doi: 10.1038/s41550-022-01812-x

Leitherer, C., Chapman, J. M., & Koribalski, B. 1997, ApJ, 481, 898, doi: 10.1086/304096

Marchenko, S. V., Moffat, A. F. J., Eenens, P. R. J., et al. 1997, ApJ, 485, 826, doi: 10.1086/304435

Marchenko, S. V., Moffat, A. F. J., Vacca, W. D., Côté, S., & Doyon, R. 2002, ApJL, 565, L59, doi: 10.1086/339138

Marois, C., Lafrenière, D., Doyon, R., Macintosh, B., & Nadeau, D. 2006, ApJ, 641, 556, doi: 10.1086/500401

Matthews, K., & Soifer, B. T. 1994, Experimental Astronomy, 3, 77, doi: 10.1007/BF00430121

Monnier, J. D., Greenhill, L. J., Tuthill, P. G., & Danchi, W. C. 2002, ApJ, 566, 399, doi: 10.1086/337961

Monnier, J. D., Tuthill, P. G., & Danchi, W. C. 1999, ApJL, 525, L97, doi: 10.1086/312352

Monnier, J. D., Tuthill, P. G., Danchi, W. C., Murphy, N., & Harries, T. J. 2007, ApJ, 655, 1033, doi: 10.1086/509873

Moran, J. P., Davis, R. J., Bode, M. F., et al. 1989, Nature, 340, 449, doi: 10.1038/340449a0

Pauls, T. A., Young, J. S., Cotton, W. D., & Monnier, J. D. 2005, PASP, 117, 1255, doi: 10.1086/444523

Pollock, A. M. T., Corcoran, M. F., Stevens, I. R., et al. 2021, ApJ, 923, 191, doi: 10.3847/1538-4357/ac2430

Ragland, S., & Richichi, A. 1999, MNRAS, 302, L13, doi: 10.1046/j.1365-8711.1999.02236.x

Richardson, N. D., Henson, M., Lieb, E. P., et al. 2025, arXiv e-prints, arXiv:2505.11616, doi: 10.48550/arXiv.2505.11616

Sander, A. A. C., Hamann, W. R., Todt, H., et al. 2019, A&A, 621, A92, doi: 10.1051/0004-6361/201833712

Serabyn, E., Huby, E., Matthews, K., et al. 2017, AJ, 153, 43, doi: 10.3847/1538-3881/153/1/43

Stevens, I. R., Blondin, J. M., & Pollock, A. M. T. 1992, ApJ, 386, 265, doi: 10.1086/171013

Tuthill, P. G., Monnier, J. D., & Danchi, W. C. 1999, Nature, 398, 487, doi: 10.1038/19033

Tuthill, P. G., Monnier, J. D., Danchi, W. C., Wishnow, E. H., & Haniff, C. A. 2000, PASP, 112, 555, doi: 10.1086/316550

Tuthill, P. G., Monnier, J. D., Lawrance, N., et al. 2008, ApJ, 675, 698, doi: 10.1086/527286

Usov, V. V. 1991, MNRAS, 252, 49, doi: 10.1093/mnras/252.1.49

Vargas Catalán, E., Huby, E., Forsberg, P., et al. 2016, A&A, 595, A127, doi: 10.1051/0004-6361/201628739

Wang, J. J., Ruffio, J.-B., De Rosa, R. J., et al. 2015,, Astrophysics Source Code Library, record ascl:1506.001

White, R. L., & Becker, R. H. 1995, ApJ, 451, 352, doi: 10.1086/176224

Williams, P. M. 1995, in IAU Symposium, Vol. 163, Wolf-Rayet Stars: Binaries; Colliding Winds; Evolution, ed. K. A. van der Hucht & P. M. Williams, 335

Williams, P. M., van der Hucht, K. A., Pollock, A. M. T., et al. 1990, MNRAS, 243, 662

Williams, P. M., Marchenko, S. V., Marston, A. P., et al. 2009, MNRAS, 395, 1749, doi: 10.1111/j.1365-2966.2009.14664.x

Xuan, W. J., Mawet, D., Ngo, H., et al. 2018, AJ, 156, 156, doi: 10.3847/1538-3881/aadae6

Yam, J. O., Dzib, S. A., Rodríguez, L. F., & Rodríguez-Gómez, V. 2015, RMxAA, 51, 35, doi: 10.48550/arXiv.1409.6484